AIAA AVIATION Forum
12-16 June 2023, San Diego, CA and Online
AIAA AVIATION 2023 Forum

10.2514/6.2023-4208

Simulation of 3D Co-Flow Jet Airfoil Control with Micro-Compressor Actuator at High Angles of Attack

Paula A. Barrios * Yan Ren † GeCheng Zha ‡
Dept. of Mechanical and Aerospace Engineering
University of Miami, Coral Gables, Florida 33124
E-mail: gzha@miami.edu

May 21, 2023

Abstract

This paper presents a 3D Co-Flow Jet (CFJ) active flow control airfoil with an integrated micro-compressor at high angles of attack for takeoff and landing conditions. A micro-compressor designed by our team is used as the fluidic actuator for CFJ active flow control (AFC). The simulations are performed at freestream Mach number 0.07 and angles of attack (AoA) from 20° to 70° to mimic takeoff and landing conditions. The RPM of the embedded micro-compressor is controlled to achieve a variety of operating conditions to satisfy the different AoA conditions. The micro-compressor actuator is designed for high efficiency at a required mass flow rate in order for the CFJ airfoil to maintain a desired momentum coefficient (C_μ). The aerodynamic performance, CFJ mass flow rate, energy expenditure, and 3D flow field are studied for the CFJ airfoil by varying the micro-compressor RPM and the CFJ airfoil AoA.

The results show that airfoil separation can occur due to the mismatch of the micro-compressor and the airfoil flow conditions. At AoA of 20°, the compressor at higher power level with 30,000 RPM stalls both the flow of the micro-compressor and airfoil. By reducing the RPM to 20,000, the CFJ airfoil flow is nicely attached with the lift coefficient doubled and the aerodynamic efficiency $(C_L/C_D)_c$ increased by 343%. With the AoA varying from 20° to 70°, increasing the RPM of the micro-compressor actuator as well as the power is necessary to overcome the extreme adverse pressure gradient to maintain attached flow with lift coefficient increasing from 3.2 to 13.7. The priority of this study is to demonstrate the functionality of the integrated CFJ airfoil system at high lift and high AoA. The efficiency is only optimized for AoA of 20°. For all the AoAs of 30° and higher, a large C_μ is used to save simulation time, without iterations to minimize the CFJ power. The aerodynamic performance of the CFJ airfoil shows a positive C_L/C_D of 111.7 and high negative values due to the generation of negative drag, which is thrust. A corrected aerodynamic efficiency $(C_L/C_D)_c$ of 13.3 is obtained for the case of $AoA = 20°$ at compressor RPM 20,000 where the micro-compressor efficiency (η) is 78.2%. The highest micro-compressor efficiency obtained is 80.2% at AoA of 40° and RPM 45,000. A high lift coefficient (C_L) of 13.7 is obtained at $AoA = 70°$ at compressor RPM 75,000 where η is 72% due to significant deviation from the design RPM of 30,000. This study indicates that the CFJ airfoil can be used for high lift coefficient with high compressor efficiency. The micro-compressor actuator designed has a wide operating range with high efficiency. This study is a virtual simulation of the integrated system of the CFJ airfoil and the micro-compressor actuator to demonstrate that the CFJ airfoil can be controlled at takeoff and landing conditions for ultra-high lift coefficient and AoA.

* Ph.D. Candidate
† Researcher. Ph.D., AIAA member
‡ Professor, ASME Fellow, AIAA associate Fellow

Nomenclature

CFJ	Co-flow jet
AoA	Angle of attack
LE	Leading Edge
TE	Trailing Edge
S	Planform area
c	Profile chord
U	Flow velocity
q	Dynamic pressure, $0.5\,\rho\,U^2$
p	Static pressure
ρ	Air density
$\dot{m}$	Mass flow rate
M	Mach number
P	Pumping power
∞	Freestream conditions
C_L	Lift coefficient, $L/(q_\infty\,S)$
C_D	Drag coefficient, $D/(q_\infty\,S)$
C_μ	Jet momentum coefficient, $\dot{m}_j\,U_j/(q_\infty\,S)$
Pc	Power coefficient, $P/(q_\infty\,S\,V_\infty)$
η	Micro-compressor total-to-total efficiency
(C_L/C_D)	Airfoil aerodynamic efficiency
$(C_L/C_D)_c$	CFJ airfoil corrected aerodynamic efficiency, $C_L/(C_D+P_c)$
$(C_L^2/C_D)_c$	CFJ airfoil cruise productivity efficiency

1 Introduction

Active flow control (AFC) transfers external energy to the controlled flow to improve the performance of the flow system. For all AFC systems, there are three measures of merit (MoM): 1) effectiveness, 2) power required (PR), and 3) power conversion efficiency (PCE). Effectiveness quantifies performance enhancement, e.g., removal of flow separation, drag reduction, lift increase, stall prevention, noise mitigation, etc. Power required quantifies the AFC power needed to achieve the targeted effectiveness. Power conversion efficiency quantifies the efficiency to convert the external energy (e.g., mechanical, electric, chemical) to energy required by the controlled flow. It determines how much total power will be consumed by the actual flow control system. For AFC to benefit industry realistic applications, all three MoM matter. The ultimate criterion for an AFC is that the system efficiency gain should be greater than the AFC energy expenditure.

Co-Flow Jet (CFJ) active flow control airfoil is shown to have high effectiveness and high energy efficiency [1, 2, 3, 4, 5, 6, 7, 8, 9, 10, 11], which are attributed to three essential factors: 1) zero-net-mass-flux as a self-contained system; 2) micro-compressor fluidic actuators with high jet momentum and high energy conversion efficiency; 3) immersed in adverse pressure gradient region with the injection near separation onset location. For the CFJ AFC, an injection slot near the leading edge (LE) and a suction slot near the trailing edge (TE) on the airfoil suction surface are created. A small amount of mass flow is withdrawn into the suction slot located near the TE, pressurized and energized by the micro-compressor, and injected near the LE tangentially to the main flow through the injection slot. CFJ is able to achieve high effectiveness and low power required. The actual power consumed by the micro-compressor is $P_{act} = P_c/\eta$, where P_c is the required power coefficient and η is the micro-compressor power conversion efficiency.

A CFJ airfoil is an integrated system with micro-compressors embedded inside as shown in Figure 1. To operate the CFJ airfoil efficiently with a wide flight range, it is crucial to understand how to achieve the desired airfoil performance by controlling the micro-compressor actuators, which are controlled by the compressor RPM. Until recently, the micro-compressor has been simulated by profile boundary conditions extracted from the micro-compressor. These boundary conditions are applied at the interface of the compressor and the duct. The simulation only reflects a specific operating condition of the micro-compressor and does not reflect the interaction effect between the micro-compressor actuator and the airfoil, which will determine the CFJ wing system operating line at different flow conditions in a flight envelope. The aerodynamic performance of the CFJ airfoil with the integrated micro-compressor actuator needs to be studied to reflect the actual compressor performance variation under different airfoil flow conditions. In particular, the compressor is designed separately with uniform inlet and outlet flow conditions. When it is embedded inside the CFJ airfoil, the flow is highly three-dimensional at the inlet and outlet. Only by simulating the CFJ airfoil and compressor together as an integrated system can it be seen how well the compressor can operate under non-uniform flow conditions.

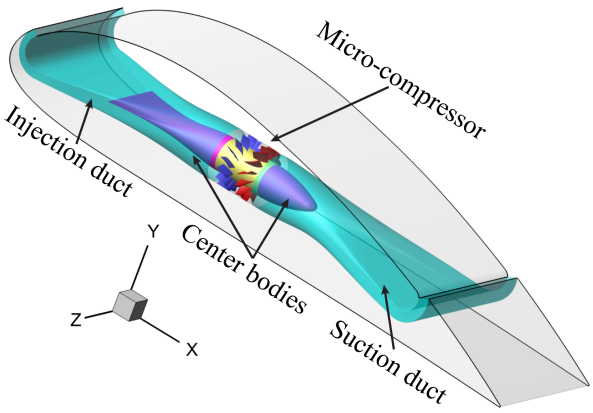

Figure 1: Schematic of CFJ setup within the airfoil

As shown in Figure 1, the suction duct connects to the micro-compressor actuator inlet and the injection duct connects to the micro-compressor outlet. The compressor is designed to achieve high efficiency at a specified mass flow rate range. This is required to achieve a desirable CFJ airfoil momentum coefficient (C_μ). To reduce the energy loss of the ducts, centerbodies are designed in both ducts to connect to the micro-compressor hub and guide the flow into and out of the compressor. Parametric studies are performed to study the CFJ airfoil and compressor performance at varying micro-compressor operating points.

Ren et al. [12] developed a high fidelity 3D CFD simulation system that integrates the CFJ airfoil with the micro-compressor actuator and the injection and suction ducts. This system is a quasi-virtual testing system to examine the integrated 3D CFJ airfoil performance. The reason that it is "quasi-" instead of a full virtual system is that at the interface of the compressor and the CFJ airfoil ducts, a circumferential average mixing boundary condition (BC) is used to achieve the compressor flow profile instead of using an unsteady sliding boundary condition. This is a typical practice in turbo-machinery steady state simulation to save CPU time. The mixing BC assumes a uniform circumferential flow, which smears the blade wake profiles, but is able to capture the primary radial work and flow distribution. When the compressor inlet flow is not uniform, with flow distortion like in the case of the CFJ airfoil, the discrepancy of using a mixing BC is expected to be increased. However, mixing BC is a reasonable and acceptable balance between accuracy and computing time. Using 3D unsteady flow simulation with a sliding BC for routine design is unfeasible at the present and foreseeable future.

The 3D flow field, pressure ratio, mass flow rate, and efficiency of the micro-compressor are controlled by varying its RPM, which further controls the airfoil performance. Barrios et al. [13] extended the simulation of Ren et

al. [12] to various Mach numbers at cruise conditions, which have low angle of attack ranging from -5° to 15°. However, CFJ aircraft may have a wide operating range with a potential angle of attack up to 70° with no stall [14]. Typically, high AoA is used at low speed short takeoff-landing conditions, which are very different from the cruise conditions in a flight envelope. No work has been done to investigate the performance of a CFJ airfoil with an embedded micro-compressor at high AoA. This knowledge is essential for CFJ aircraft design with a wide operating range.

The ultimate goal of this effort is to investigate how to control the system for a high lift coefficient by increasing the compressor RPM. In doing so, a lower C_μ and lower P_c are not the focus here but will be the next step for design optimization. The purpose of this paper is to use the quasi-virtual system and investigate the operating performance of the micro-compressor actuators at high AoA and low speed ($M = 0.07$) short takeoff-landing conditions. It will examine the compressor operating range and the CFJ airfoil flow behavior at high AoA with the flows provided by the compressor. Together with the previous study for cruise conditions [13], this research will provide a more complete performance of the CFJ airfoil for the entire flight envelope including takeoff, landing, and cruise.

2 Methodology

2.1 Lift and Drag Calculation

In a CFD analysis of a CFJ airfoil, the total aerodynamic forces and moments are determined by the force surface integral and jet reactionary force. The reactionary force of a CFJ airfoil is calculated through flow parameters obtained from the injection and suction slots. The equations for lift and drag due to the jet reactionary force are given by Zha et al. [2] using the control volume analysis in Figure 2:

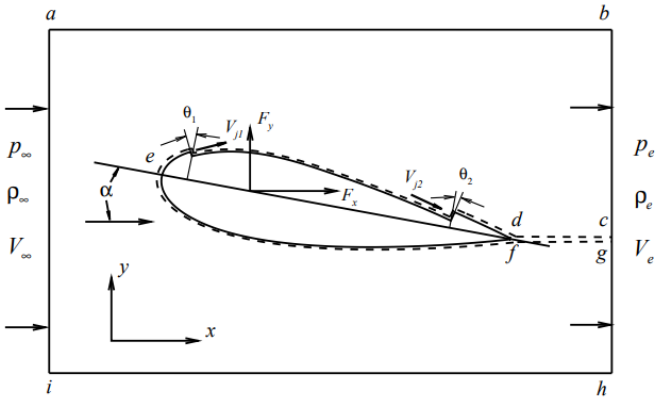

Figure 2: Control volume of a CFJ airfoil

$$F_{x_{cfj}} = (\dot{m}_j V_{j1} + p_{j1} A_{j1}) * cos(\theta_1 - \alpha) - (\dot{m}_j V_{j2} + p_{j2} A_{j2}) * cos(\theta_2 + \alpha) \tag{1}$$

$$F_{y_{cfj}} = (\dot{m}_{j1} V_{j1} + p_{j1} A_{j1}) * sin(\theta_1 - \alpha) + (\dot{m}_{j2} V_{j2} + p_{j2} A_{j2}) * sin(\theta_2 + \alpha) \tag{2}$$

where the subscript 1 indicates the injection slot and subscript 2 denotes the suction slot, θ_1 and θ_2 are the angles between the slot's surface and a line normal to the chord, and α is the angle of attack.

Total lift and drag are given by the following equations:

$$D = R'_x - F_{x_{cfj}} \tag{3}$$

$$L = R'_y - F_{y_{cfj}} \tag{4}$$

where R'_x and R'_y are surface integrals of pressure and shear stress in the x_{drag} and y_{lift} directions. For a 3D CFJ wing, total lift and drag are determined by integrating the drag and lift equations in the spanwise direction.

2.2 Jet Momentum Coefficient

C_μ, or the jet momentum coefficient, quantifies the jet intensity and is defined by,

$$C_\mu = \frac{\dot{m}V_j}{\frac{1}{2}\rho_\infty {V_\infty}^2 S} \tag{5}$$

where $\dot{m}$ is the injection mass flow rate, V_j is the mass-averaged injection velocity, ρ_∞ is the freestream density, V_∞ is the freestream velocity, and S is the planform area. In this study, the CFJ injection momentum coefficient is controlled by the micro-compressor RPM that also determines the micro-compressor power.

2.3 Micro-Compressor Power Coefficient

In a CFJ airfoil, a system of micro-compressors are embedded inside of the wing. The micro-compressors take air from the suction slot and and eject the air through the injection slot. The power consumption is determined by the jet mass flow and total enthalpy change through:

$$P_{CFJ} = \dot{m}(H_{t1} - H_{t2}) \tag{6}$$

where H_{t1} and H_{t2} are the mass-averaged total enthalpy in the injection and suction slots, P is the power required by the micro-compressor, and $\dot{m}$ the jet mass flow rate. The power consumption of Eq. (6) can be also expressed by the following equation,

$$P_{CFJ} = \frac{\dot{m}C_pT_{t2}}{\eta}(\Gamma^{\frac{\gamma-1}{\gamma}} - 1) \tag{7}$$

where γ is the specific heat ratio, or 1.4 for ideal gas, and η is the isentropic pumping efficiency. Γ is the total pressure ratio of the pump defined as $\Gamma = \frac{P_{t1}}{P_{t2}}$, where P_{t1} and P_{t2} are the mass-averaged total pressures in the injection and suction slots, respectively. The power coefficient for a CFJ airfoil is then,

$$P_{C,CFJ} = \frac{P_{CFJ}}{\frac{1}{2}\rho_\infty V_\infty^3 S} \tag{8}$$

The micro-compressor isentropic efficiency is defined by,

$$\eta = \frac{\Gamma^{\frac{\gamma-1}{\gamma}} - 1}{\frac{T_{t1}}{T_{t2}} - 1} \tag{9}$$

where T_{t1} and T_{t2} are the total temperatures in the injection and suction slots respectively.

2.4 Corrected Aerodynamic Efficiency

For a conventional airfoil, the wing aerodynamic efficiency is defined as:

$$\frac{L}{D} \tag{10}$$

and for a CFJ wing, the pure aerodynamic relationship between lift and drag still follows Eq. 10. However, since CFJ AFC expends energy, the above is modified to consider the energy consumption of the micro-compressor. The corrected aerodynamic efficiency is:

$$\frac{C_L}{C_{Dc}} = \frac{C_L}{C_D + P_C} \tag{11}$$

where C_{Dc} is the equivalent drag coefficient that includes the drag of the aircraft system and the power required by the CFJ.

2.5 Aircraft Productivity

The productivity efficiency C_L^2/C_D is used to measure the productivity of an airplane characterized by the product of an aircraft's range and its weight [14]. It is a more thorough parameter than C_L/C_D in determining the merit of aerodynamic design during cruise. Aircraft productivity includes the ratio of lift to drag coefficient and the aircraft weight from C_L. The corrected productivity efficiency for CFJ airfoils is defined as,

$$\frac{C_L^2}{C_{Dc}} = \frac{C_L^2}{C_D + P_c} \tag{12}$$

2.6 Airfoil Geometry

The airfoil is developed based on the NACA 6421 airfoil. The CFJ injection and suction slot sizes are normalized by the airfoil chord length (C). The original airfoil design, CFJ6421-SST150-SUC247-INJ117, created by Wang et al. [15, 16, 17] was used as a starting point. It has an injection slot size of 1.17%C and suction slot size of 2.47%C. However, during design iterations, the suction slot height was decreased by 30% to reduce flow separation occurring within the duct. The current airfoil used in this study is CFJ6421-SST150-SUC173-INJ117.

2.7 CFD Simulation Setup

The FASIP (Flow-Acoustics-Structure Interaction Package) CFD code is used for the numerical simulation. The 3D Reynolds Averaged Navier-Stokes (RANS) equations with one-equation Spalart-Allmaras [18] turbulence model is used. A 3rd order WENO scheme for the inviscid flux [19, 20, 21, 22, 23, 24] and 2nd order central differencing for the viscous terms [19, 23] are utilized to discretize the Navier-Stokes equations. The low diffusion E-CUSP scheme used as the approximate Riemann solver suggested by Zha et al. [20] is utilized with the WENO scheme to evaluate the inviscid fluxes. Implicit time marching method using Gauss-Seidel line relaxation is used to achieve a fast convergence rate [25]. Parallel computing is implemented to save wall clock simulation time [26]. The micro-compressor rotor flow is simulated in the rotating frame while the stator, the CFJ airfoil, and ducts are simulated in the stationary frame. In the rotating frame, the centrifugal and Coriolis forces are included as described in [27, 28]. The flows of the airfoil and compressor are iterated via the mixing boundary conditions until the whole flow field is converged.

2.8 Boundary Conditions

The 3rd order accuracy no slip condition is enforced on the solid surface with the wall treatment suggested in [29] to achieve flux conservation on the wall. Symmetric boundary conditions are utilized on the two boundaries

in the span direction to ensure the effect of a segment of a 3D CFJ wing. Total pressure, total temperature, and flow angles are specified at the upstream portion of the far field. Constant static pressure is applied at the downstream portion of the far field. Mixing plane boundary conditions are applied at the interfaces of the ducts and the micro-compressor. Cross-sectional faces of the ducts are meshed with an "H" topology while the mesh around the airfoil uses an "O" topology. The total mesh size, shown in Figure 3(a) is 7.225 million grid cells, split into 168 blocks for the parallel computation. Figure 3(b) shows the details of the compressor mesh simulated using steady state mixing boundary conditions between the rotor and stator blades and the interface with the CFJ injection and suction duct. The first grid point on the wing surface is placed at $y^+ \approx 1$.

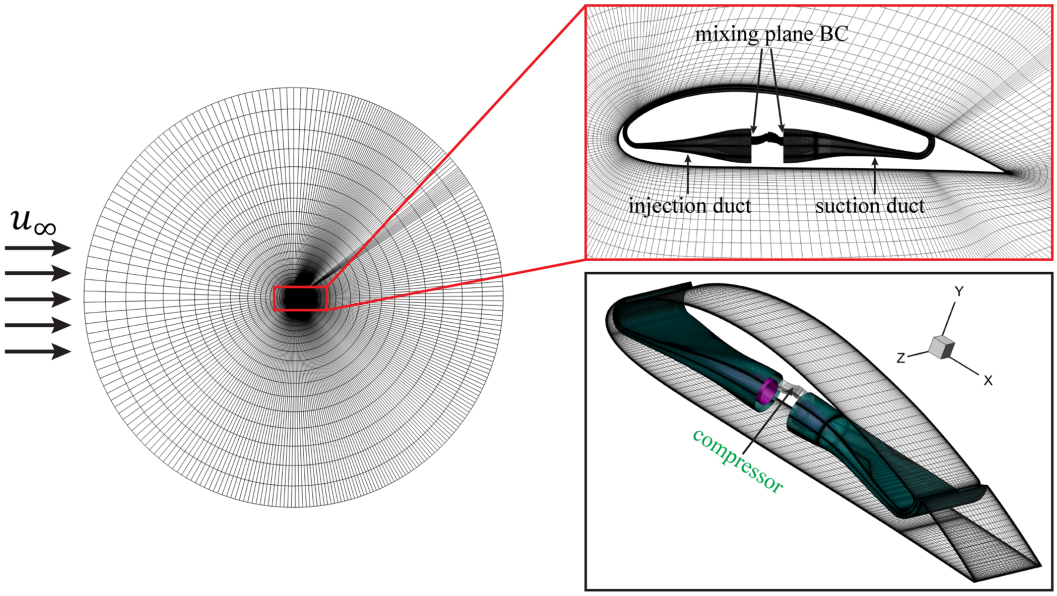

(a)

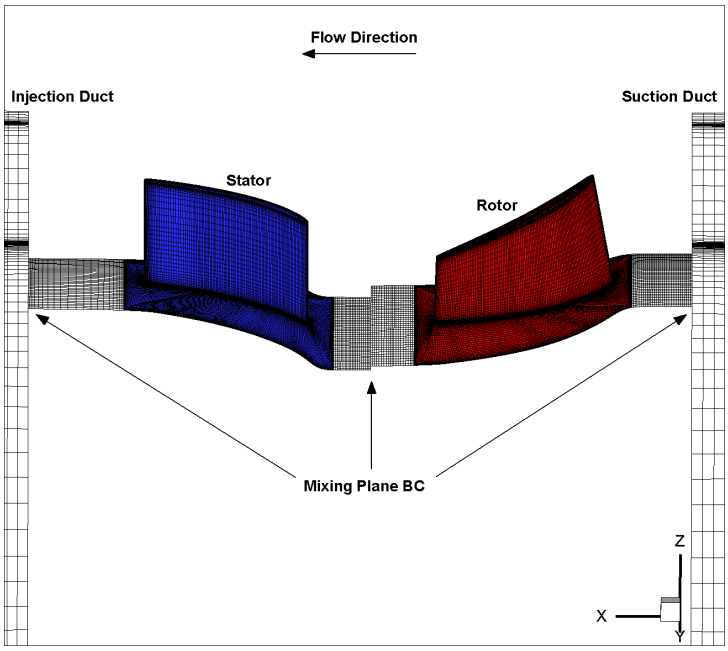

(b)

Figure 3: Computational mesh: (a)far field and airfoil with ducts and compressor, and (b)detailed compressor

2.9 Steps for the Integrated Design

The integrated design steps are as follows:

1. CFJ wing design: 2D CFJ airfoil and 3D CFJ wing are designed to meet the aircraft mission requirements for takeoff, cruise, and landing with optimal performance. The design provides the requirements of wing dimensions, micro-compressor mass flow rate, and total pressure ratio.

2. Micro-compressor design: A micro-compressor is then designed to satisfy the required total pressure ratio and the dimensions of the airfoil with maximized mass flow rate, highest efficiency, and largest operating range from choke limit to stall limit.

3. Duct design: The CFJ injection and suction ducts are then designed to match the airfoil dimensions with the boundary conditions from the micro-compressor and the CFJ wing flow conditions, no flow separation inside the ducts, and minimum total pressure loss.

4. Integrate the ducts with the 3D CFJ airfoil and the micro-compressor connected to the CFJ injection inlet (micro-compressor outlet) and suction outlet (micro-compressor inlet). Simulate the 3D CFJ airfoil with the embedded micro-compressor which is controlled by the RPM.

5. Examine the results and the aerodynamic performance. If satisfied, the design is complete; if not satisfied, return to Step 1 and repeat the process.

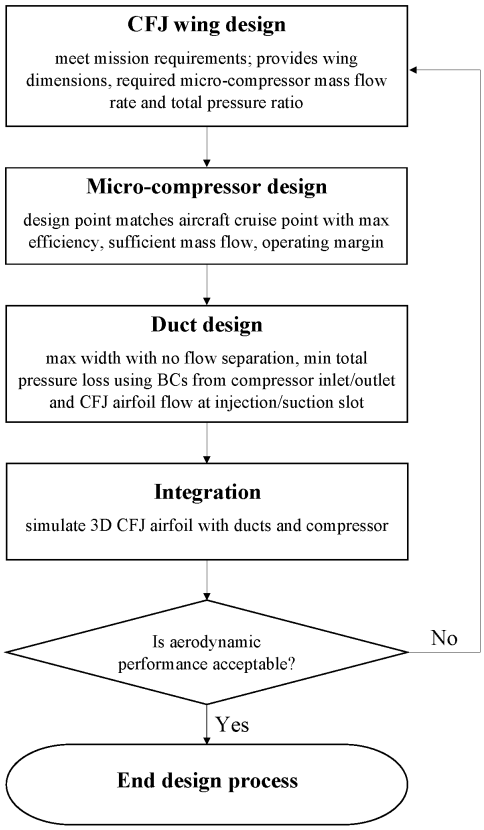

Figure 4: Flowchart of the integrated design process

This paper conducts Steps 4 and 5 with the micro-compressor actuator.

3 Results and Discussion

The CFJ airfoil and micro-compressor performances are examined under various operating conditions. The micro-compressor actuator, namely G8 actuator, is designed by our team for CoFlow Jet airfoil flow control to have broad operating range and high efficiency [30]. The corresponding parameters of the micro-compressor employed are listed in Table 1. Simulations are conducted at freestream Mach number 0.07 for $AoA = 20^\circ$, 30°, 40°, 50°, 60°, and 70°. The compressor RPM is varied to remove any flow separation. Changing the RPM also changes the jet momentum coefficient so that increasing C_μ results in higher lift coefficient. The primary goal is to obtain a high lift coefficient, consequently the C_μ and P_c reported for $AoA = 30^\circ$ - 70° are not optimized. The following figures show flow fields for various operating conditions with flow in the compressor in the positive x direction.

Table 1: Micro-compressor specifications

Design RPM	30,000
Design mass flow rate	0.165 kg/s
Design total pressure ratio	1.04
Design efficiency	84.4%
Outer Diameter	64 mm
Number of stages	1

At $AoA = 20^\circ$, the compressor design RPM of 30,000 is used initially. However, the compressor operating in that condition is overloaded and stalled with separation occurring at the stator blades as shown in Figure 5(a). The RPM is then decreased to shift the compressor to a lower speedline and lower power condition. Figure 5(b) shows that at 20,000 RPM the compressor is no longer stalled and the separation is removed, with the flow well attached. Table 2 quantifies the results of operating the compressor at 30,000 and 20,000 RPM. The former results in low lift, high drag, a low mass flow rate of 0.074 kg/s, and a high total pressure ratio of 1.025. Decreasing the RPM increases the mass flow rate to 0.099 kg/s and decreases the total pressure ratio to 1.018. It also increases the C_μ by 80%, almost doubles the C_L, decreases C_D and P_c by 85% and 40.5% respectively, improves the compressor efficiency from 47.3% to 78.2%, and increases C_L/C_{D_c} by 343%. This case shows how important it is to match the compressor operating condition with the airfoil flow condition to achieve a high overall CFJ system performance and efficiency. Simply increasing the compressor power may not improve the CFJ airfoil performance, but may jeopardize it.

Table 2: Simulation results for $AoA = 20^\circ$at $M = 0.07$

AoA	RPM	C_μ	C_L	C_D	P_c	$\frac{C_L}{C_D}$	$(\frac{C_L}{C_D})_c$	$(\frac{C_L^2}{C_D})_c$	P_{tr}	T_{tr}	$\dot{m}$ (kg/s)	η (%)
20°	30,000	0.1103	1.70	0.1988	0.3594	8.5	3.0	5.2	1.025	1.015	0.074	47.3
20°	20,000	0.1983	3.23	0.0289	0.2140	111.7	13.3	42.9	1.018	1.007	0.099	78.2

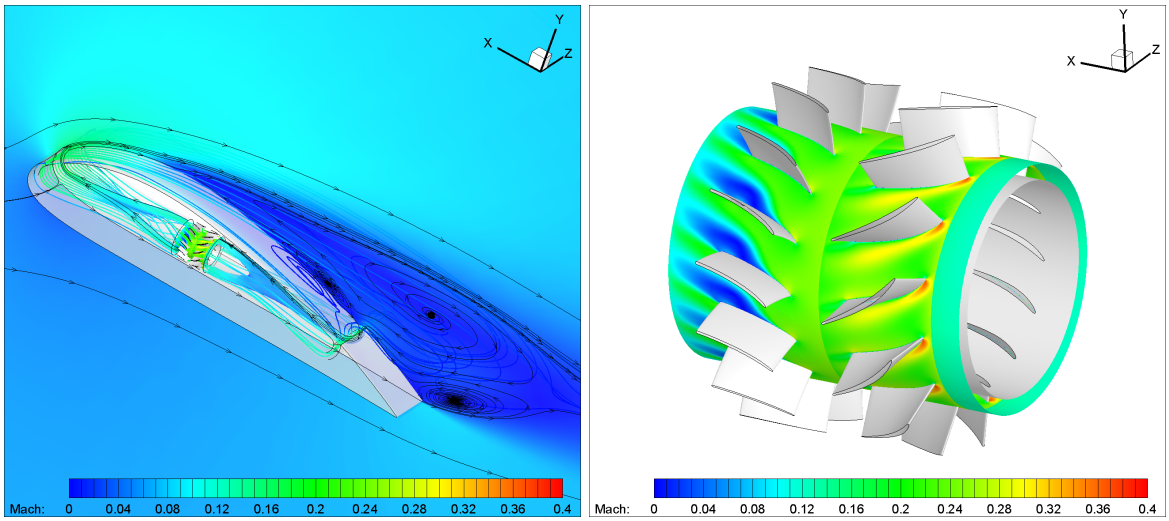

(a)

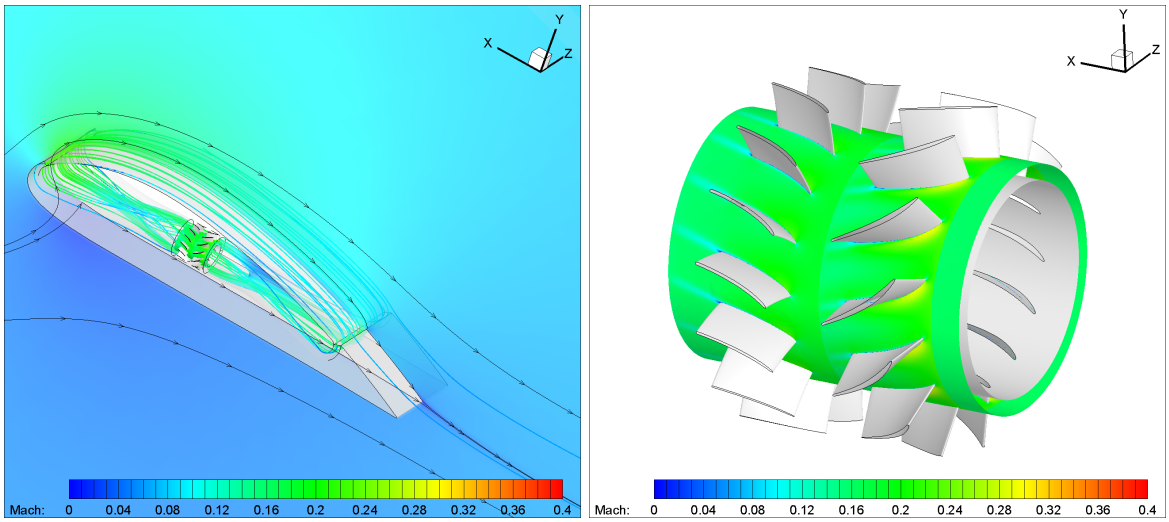

(b)

Figure 5: Flow fields of airfoil midspan and compressor 25% span location at $AoA = 20°$ for (a)RPM 30,000, and (b)RPM 20,000

Figure 6 displays additional flow fields for $AoA = 20°$. The flow within the ducts, as shown in Figure 6(a), gains momentum with the higher mass flow increasing the jet momentum. Above the suction duct centerbody there is a region of weak flow but there is no separation. Figures 6(b) and (c) show the compressor flow field at 25% and 95% span respectively. The compressor does not show any separation and the maximum Mach number is 0.32 at the rotor tip region.

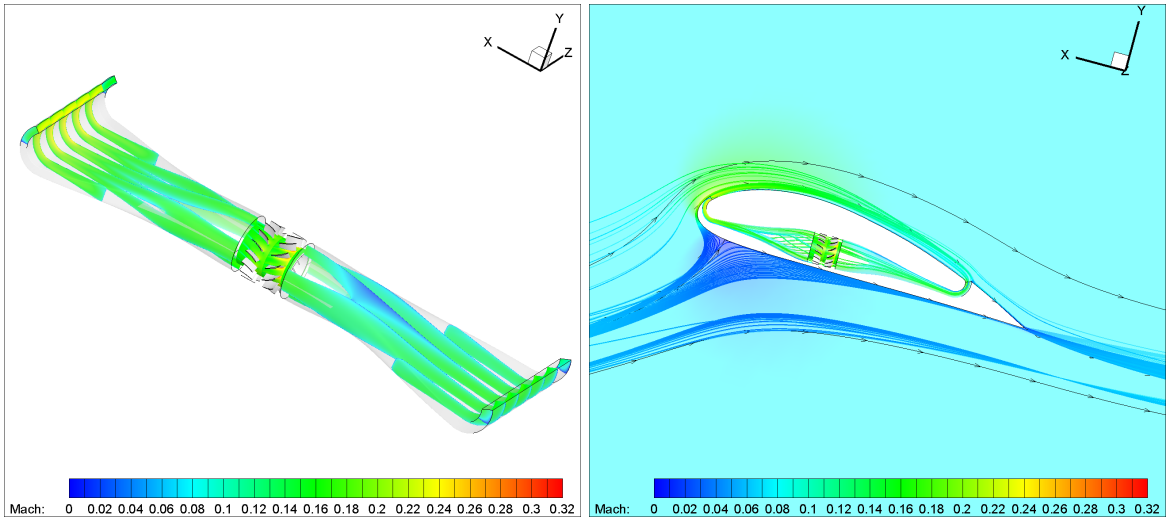

(a)

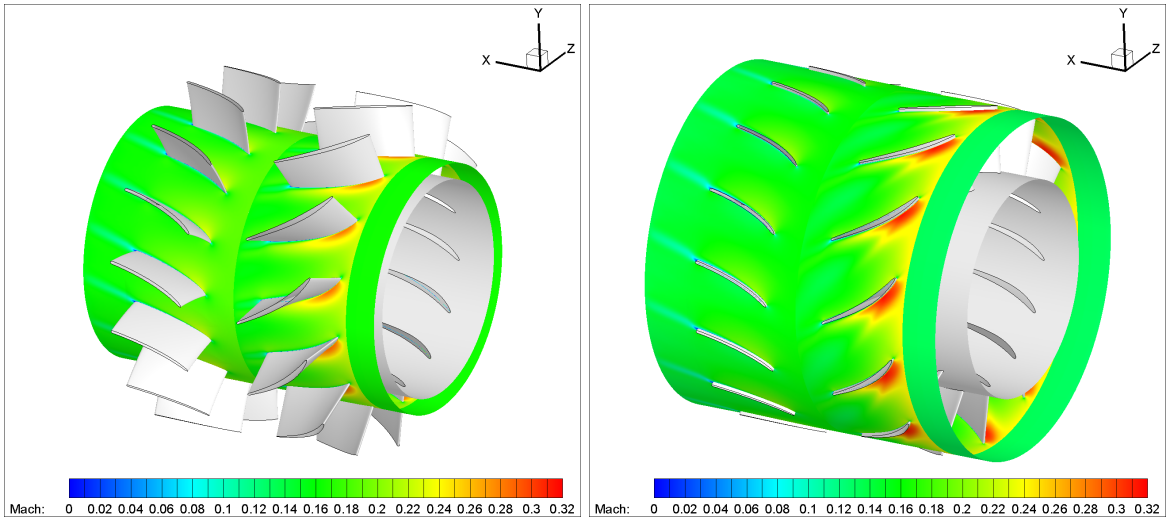

(b) (c)

Figure 6: Mach contours of $AoA = 20°$ and 20,000 RPM: (a)Z slices of injection and suction ducts and flow at 50% airfoil midspan, (b)25% compressor span, and (c)95% compressor span

At $AoA = 30°$, the compressor RPM is increased to 35,000. At an RPM of 35,000 the integrated CFJ airfoil and compressor simulation results in a C_μ of 0.56. Figures 7(a) show the overall 3D flow and streamlines colored by Mach number for the midspan section. They indicate that the flow field is well attached to the airfoil with the stagnation point moving downstream farther from the leading edge on the pressure surface. The contours at the 50% span location show a weaker flow above the suction duct centerbody but the streamlines in the ducts do not show separation. Figure 7(b) shows the flow field at the 25% span location for the compressor with healthy flow and no separation. Figure 7(c) shows the 95% span location with a maximum Mach number of 0.56 and no flow separation so that the compressor operates at a high efficiency of 79.9%.

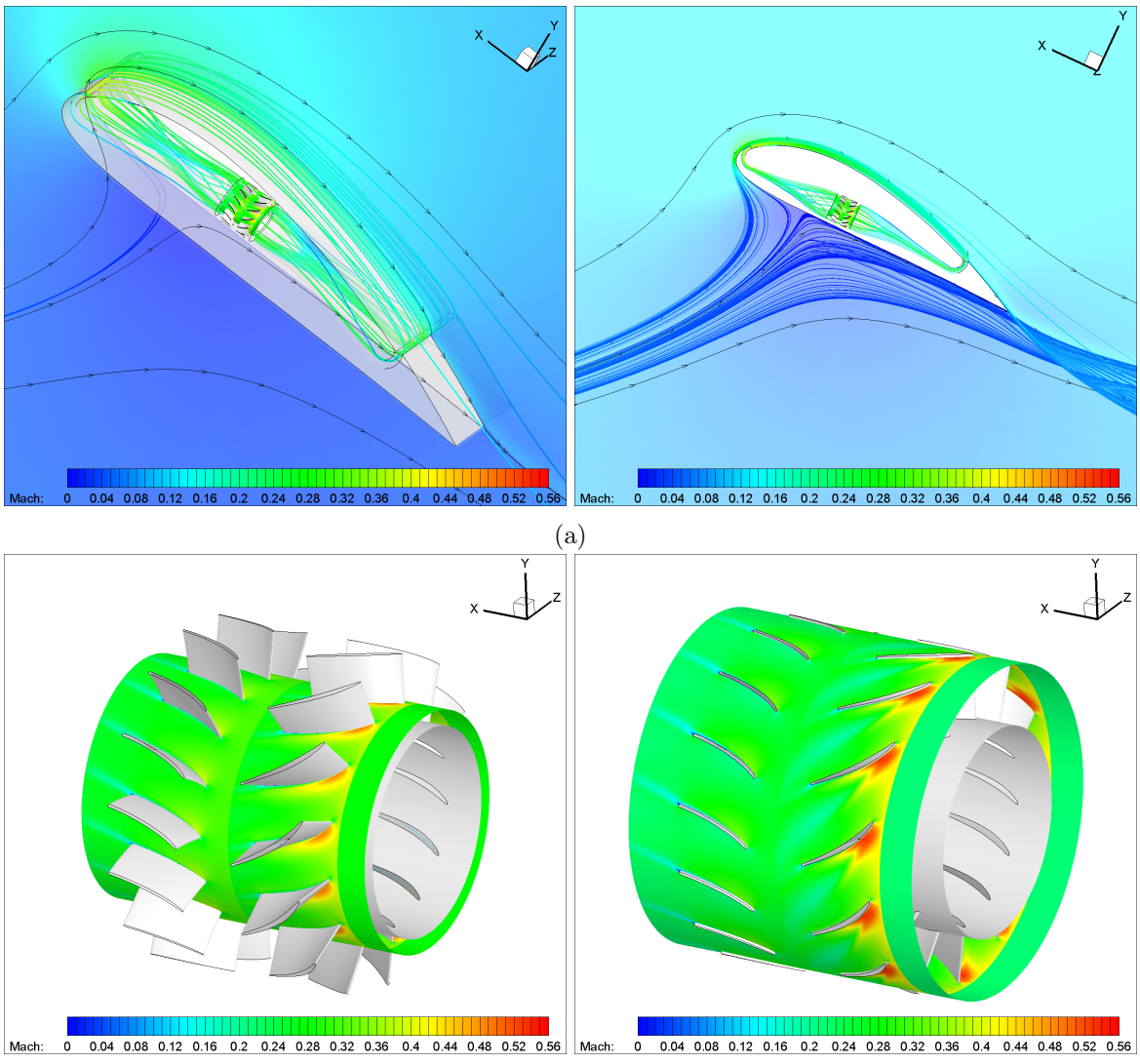

Figure 7: Mach contours of $AoA = 30°$ and 35,000 RPM: (a)3D flow and flow at 50% airfoil midspan, (b)25% compressor span, and (c)95% compressor span

At $AoA = 40°$, the compressor RPM is 45,000 with C_μ of 0.91 and the flow remains attached with C_L of 6.75. Figures 8(a) show the overall 3D flow field and the flow at the airfoil midspan. The streamlines show the flow is well attached over the airfoil surface. Compared with the flow at AoA of 30° as shown in Figure 7(a), the stagnation point on the airfoil pressure surface continues to shift toward the trailing edge. Figures 8(b) and (c) display the Mach contours at the compressor 25% and 95% span, the flow does not have any separation and the maximum Mach number is 0.73 at the rotor tip region, for a compressor efficiency of 80.2%.

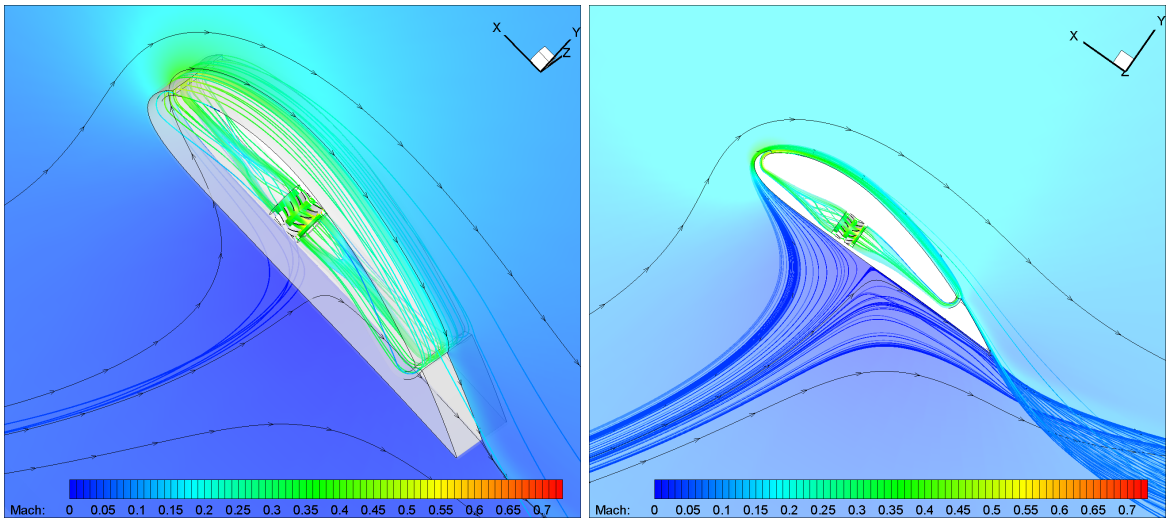

(a)

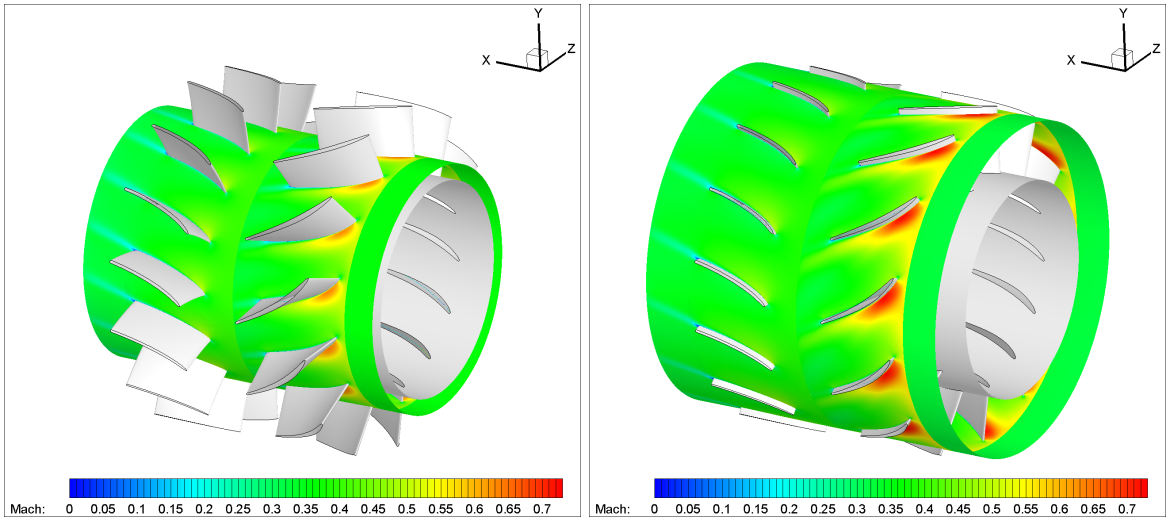

(b) (c)

Figure 8: Mach contours of $AoA = 40°$ and 45,000 RPM: (a)3D flow and flow at 50% airfoil midspan, (b)25% compressor span, and (c)95% compressor span

At $AoA = 50°$, the compressor RPM is increased to 60,000 with the C_μ increased to 1.457 to maintain flow attachment with a high lift coefficient of 9.22. Figures 9(a) show the 3D flow field and Mach contours at the midspan of the airfoil with streamlines around the airfoil and through the injection and suction ducts. The flow is well attached on the airfoil and the internal duct streamlines do not show any separation. The stagnation point on the airfoil pressure surface moves close to the trailing edge. Figure 9(b) is the compressor at the 25% span location near the hub. The compressor shows separation at the stator but otherwise healthy flow is still maintained at this RPM. Figure 9(c) is the compressor at the 95% span location with no flow separation at the stator blade. The rotor tip region reaches slightly supersonic speeds with a maximum Mach number 1.02 near the leading edge.

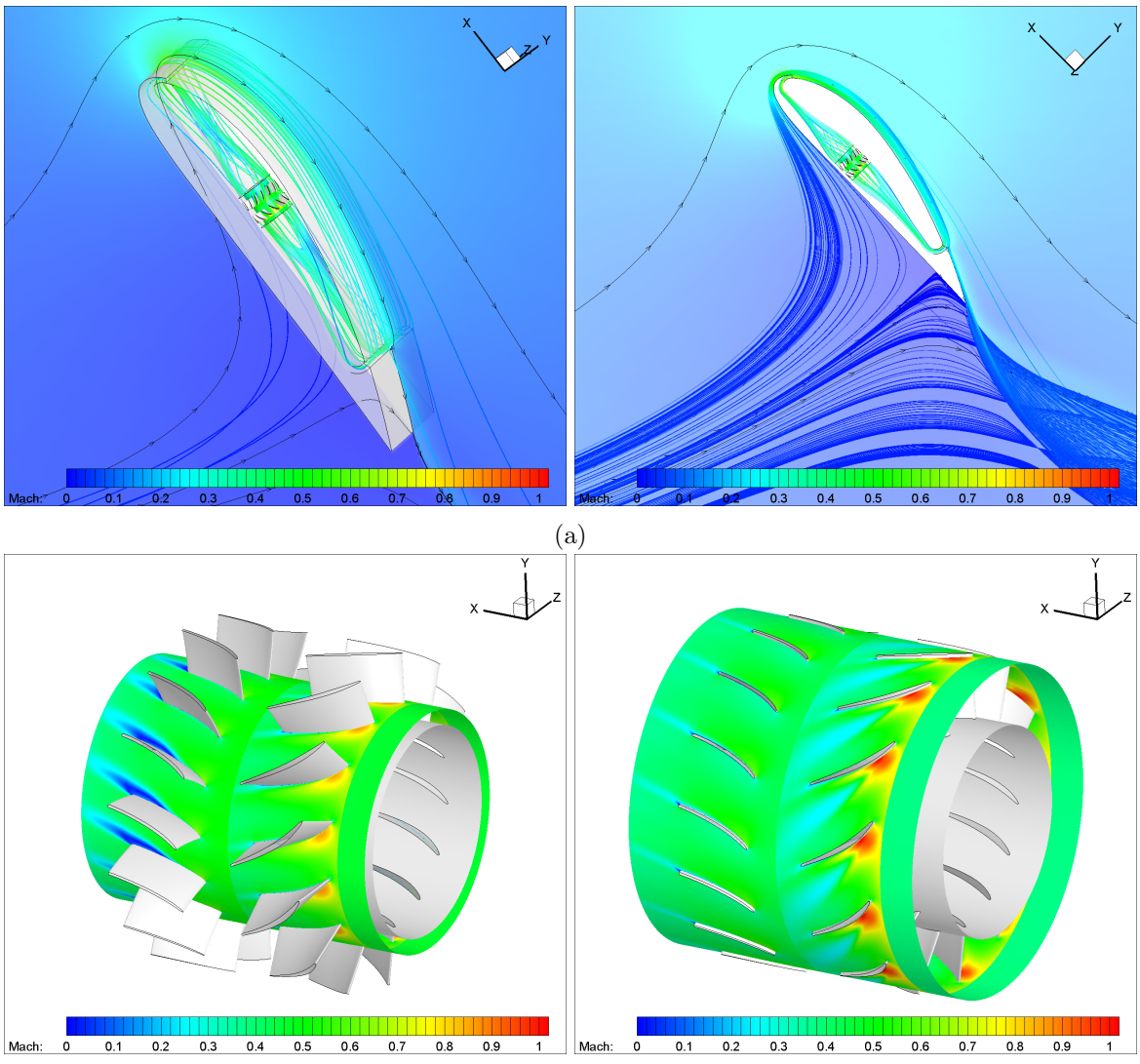

Figure 9: Mach contours of $AoA = 50°$ and 60,000 RPM: (a)3D flow and flow at 50% airfoil midspan, (b)25% compressor span, and (c)95% compressor span

At $AoA = 60°$, the compressor RPM is further increased to 65,000 with a C_μ of 1.7 to attach the flow that has a C_L of 11.1. Figures 10(a) show the Mach contours of the 3D flow field and the flow at the airfoil midspan along with streamlines. At this angle of attack, the stagnation point on the airfoil pressure surface is very close to the trailing edge with streamlines going around the entire airfoil. Figures 10(b) and (c) show the compressor Mach contours at the 25% and 95% span locations, respectively. The compressor shows separation at the stator blade near the hub. At the rotor tip region, the maximum Mach number is increased to 1.21 but the flow is not choked.

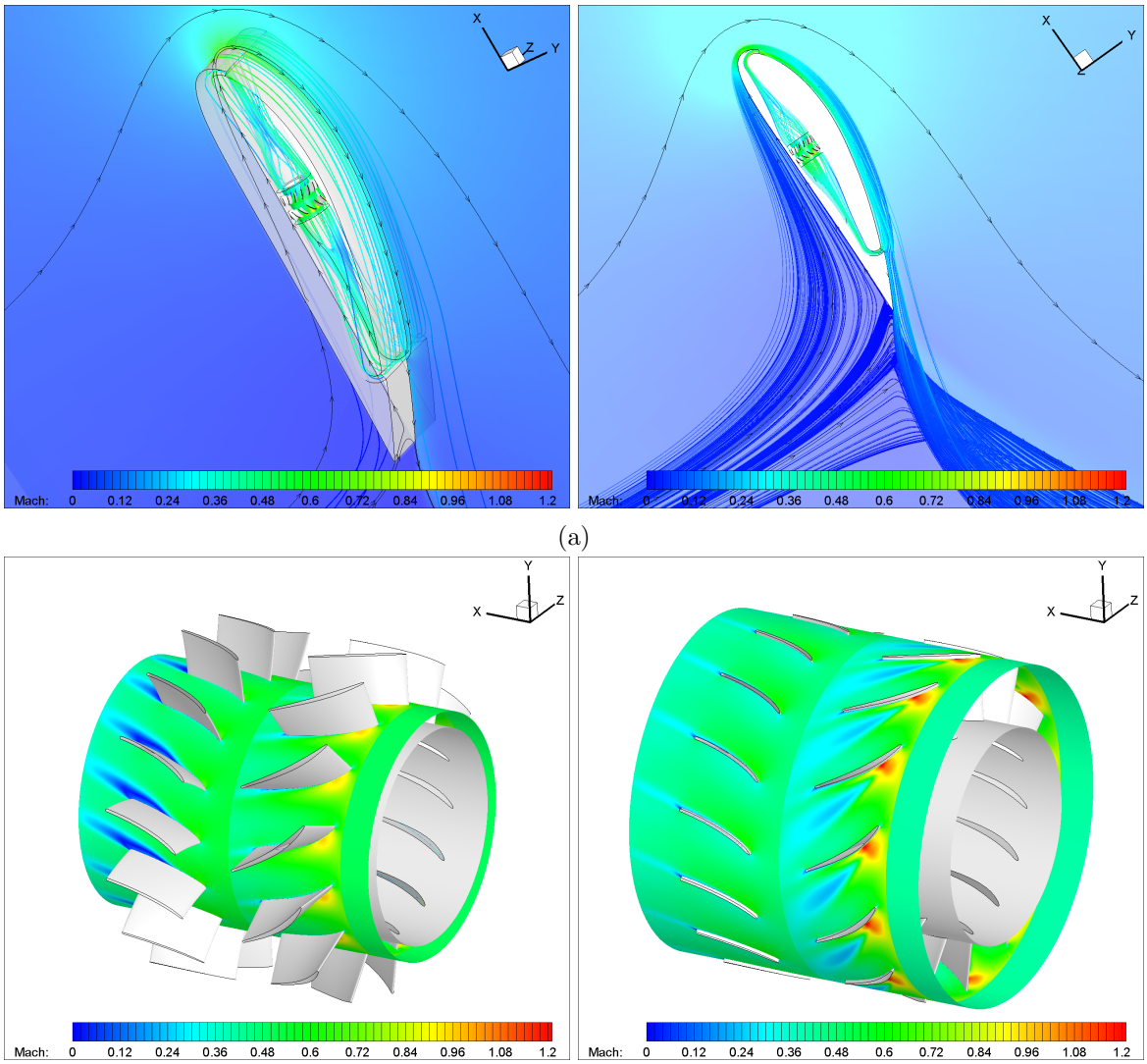

(a)

(b) (c)

Figure 10: Mach contours of $AoA = 60°$ and 65,000 RPM: (a)3D flow and flow at 50% airfoil midspan, (b)25% compressor span, and (c)95% compressor span

At $AoA = 70^{\circ}$, the compressor RPM is increased to 75,000 with a C_{μ} of 1.94 and the flow is still attached with a C_L of 13.73. Figures 11(a) and (b) show the Mach contours of the overall 3D flow and the flow at the 50% airfoil midspan with streamlines showing a second stagnation point detached from the solid body of the airfoil. The detached stagnation point is stable since the lift and drag do not oscillate. Figures 11(c) and (d) are sections along the airfoil span at 25% and 75% respectively. These show the stagnation vortex has some three-dimensionality, which is attributed to the swirl effect of the flow coming out of the micro-compressor. Figure 12 is the compressor Mach contours at the 25%, 75%, 90%, and 95% span locations. Near the hub at 25% span there is separation at the stator blade. At 75% span the stator separation disappears with high speed flow at the rotor. At the 90% span location there is weak flow separation near the rotor trailing edge. The maximum Mach number is 1.32 and occurs at the 95% span rotor tip region where the flow is more severely separated. This appears to be because RPM of 75,000 is quite far away from the design RPM of 30,000. The compressor rotor is more loaded with higher incidence near the tip that creates flow separation. The compressor efficiency drops to 72%. Overall, this micro-compressor designed by our team [30] demonstrates a very broad operating range with high efficiency.

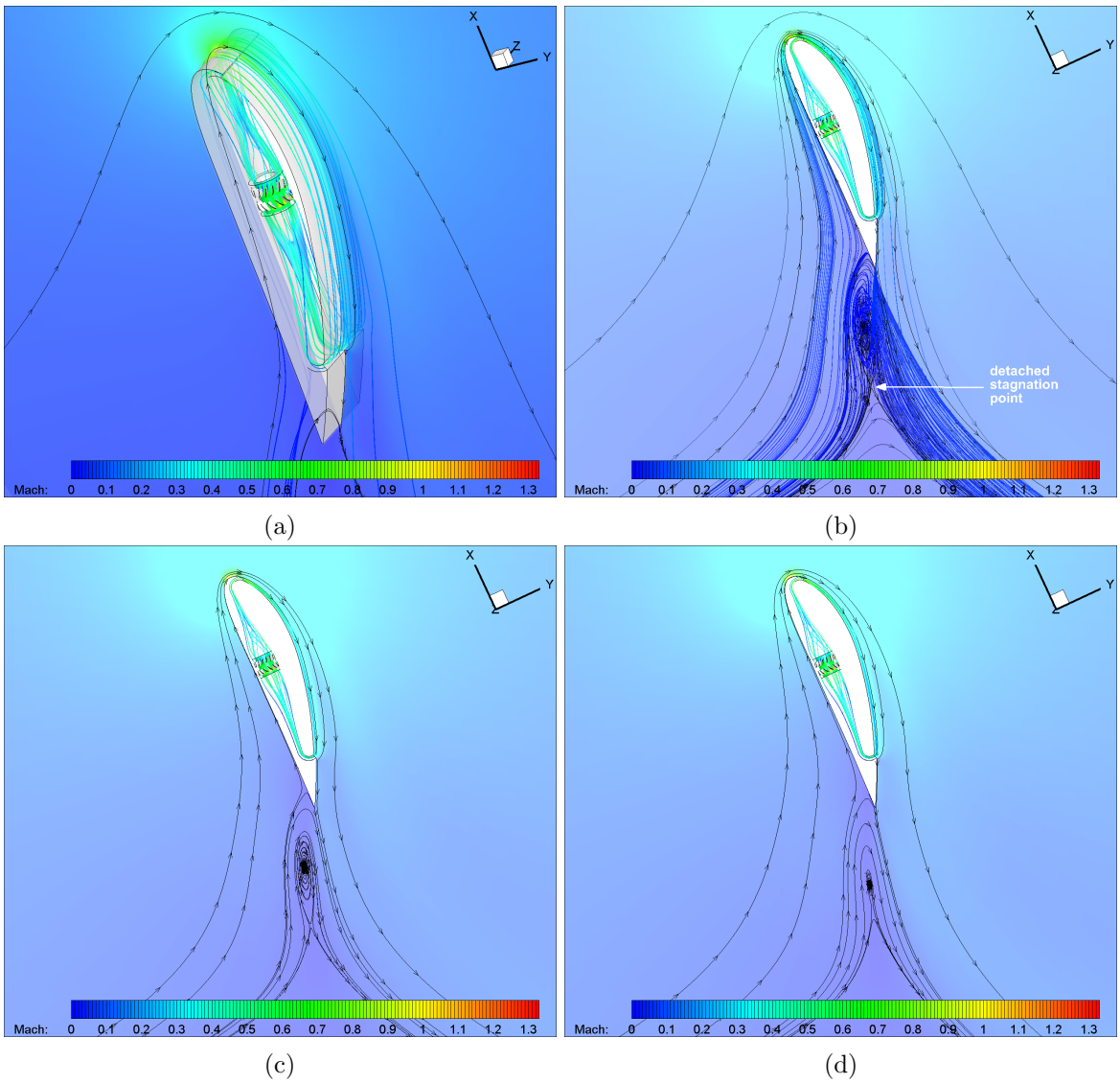

Figure 11: Mach contours of $AoA = 70^{\circ}$ and 75,000 RPM: (a)3D flow, (b)flow at 50% airfoil midspan, (c)25% airfoil span, and (d)75% airfoil span

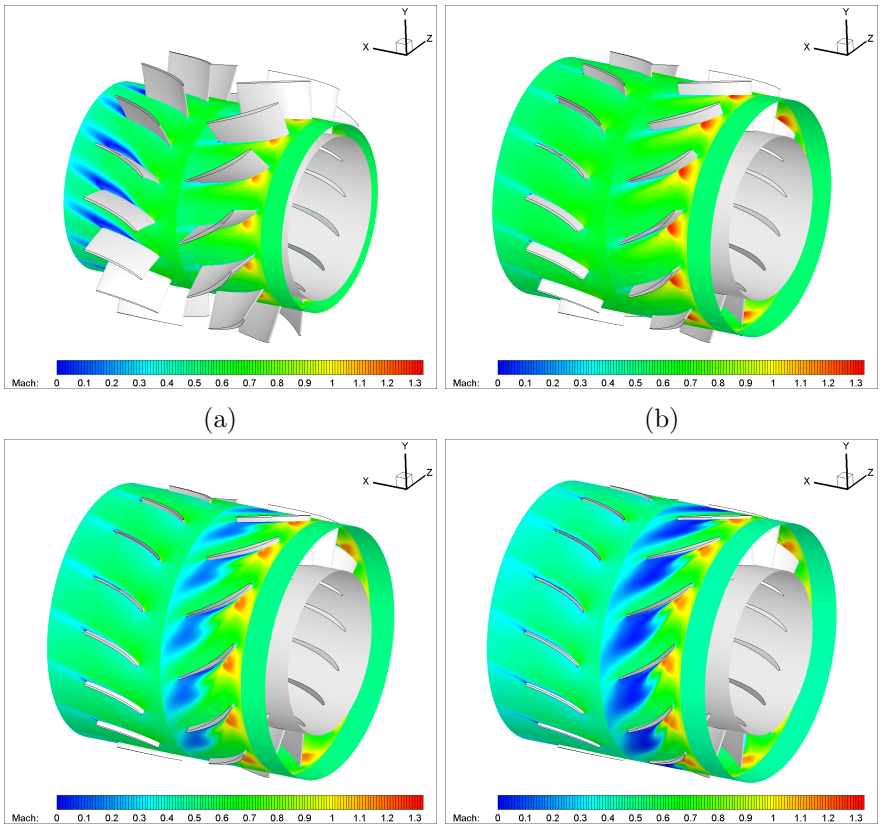

Figure 12: Compressor contours of $AoA = 70°$ and 75,000 RPM at (a)25%, (b)75%, (c)90%, and (d)95% span

Table 3 shows the results of the CFJ airfoil and compressor performance for $M = 0.07$ at AoAs between 20° and 70°, with RPMs ranging from 20,000 to 75,000. The lift coefficients observed range from 3.2 to 13.7. The drag coefficient becomes negative, indicating the generation of thrust, for the AoA greater than 30°. Increasing AoA requires increasing the compressor RPM which in turn results in higher C_μ and power coefficient P_c. Higher compressor power requires larger total pressure ratio of the compressor as well as an increase in the total temperature ratio and mass flow rate. The compressor has a maximum efficiency of 80.2% at $AoA = 40°$ with 45,000 RPM. At higher RPMs the efficiency starts decreasing as the compressor rotor tip speed increases past Mach 1. Even though the corrected aerodynamic efficiency ($(C_L/C_D)_c$) drops with increasing AoA, the integrated CFJ system can operate well at high AoAs where most conventional aircraft would stall while still resulting in a high C_L.

Table 3: Simulation results for $M = 0.07$

AoA	RPM	C_μ	C_L	C_D	P_c	$\frac{C_L}{C_D}$	$(\frac{C_L}{C_D})_c$	$(\frac{C_L^2}{C_D})_c$	P_{tr}	T_{tr}	$\dot{m}$ (kg/s)	η (%)	Power (W)
20°	20,000	0.198	3.23	0.029	0.214	111.7	13.3	42.9	1.018	1.007	0.099	78.2	173
30°	35,000	0.564	5.01	-0.046	1.141	-109.2	4.6	23.0	1.059	1.021	0.162	79.9	920
40°	45,000	0.907	6.75	-0.096	2.370	-70.2	3.0	20.0	1.099	1.034	0.201	80.2	1912
50°	60,000	1.457	9.22	-0.194	5.297	-47.5	1.8	16.7	1.177	1.061	0.246	78.4	4273
60°	65,000	1.699	11.10	-0.141	6.552	-78.6	1.7	19.2	1.204	1.071	0.259	77.4	5285
70°	75,000	1.939	13.73	-0.054	8.851	-253.2	1.6	21.4	1.249	1.091	0.265	72.4	7140

Figure 13(a) shows that the compressor mass flow rate linearly increases with RPM. Figure 13(b) shows the compressor power also varies with RPM with the slope becoming steeper when the RPM is greater than 45,000. The power increases substantially after 45,000 RPM. Achieving a high lift coefficient requires significant compressor power. Figure 13(c) shows the CFJ airfoil jet momentum coefficient (C_μ) and the micro-compressor power coefficient (P_c) at different operating points. C_μ and P_c increase with increasing micro-compressor $\dot{m}$. The power coefficient increase is due to both the increase in mass flow rate and total pressure ratio from the increasing micro-compressor RPM. Figure 13(d) shows the total pressure ratio (P_{tr}) and efficiency (η) at different operating points. P_{tr} increases with compressor RPM and therefore the $\dot{m}$. The peak compressor η of 80.2% is achieved at RPM of 45,000 and AoA of 40°.

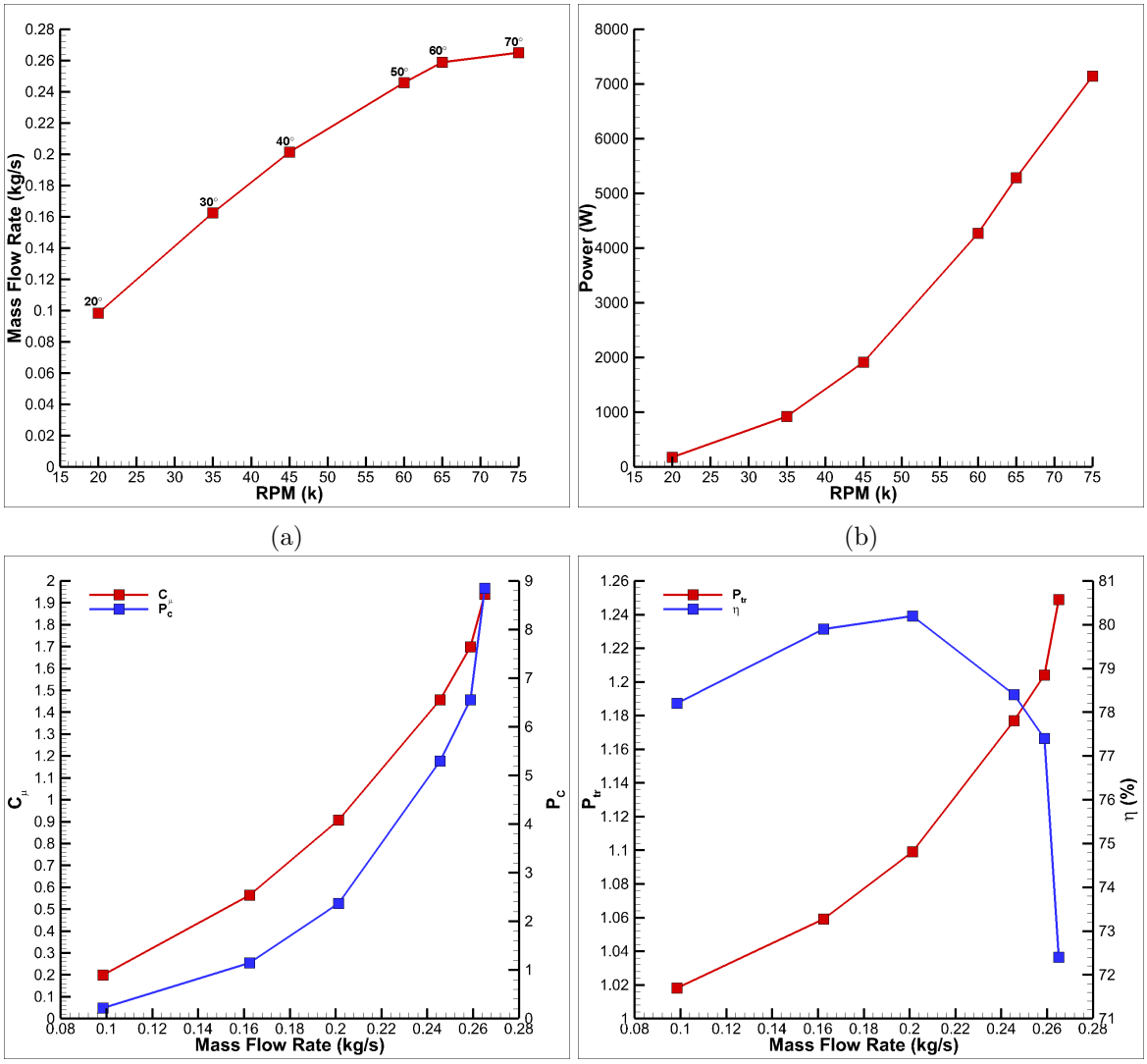

Figure 13: Compressor performance: (a)RPM vs $\dot{m}$, (b)RPM vs Power, (c)$\dot{m}$ vs C_μ & P_c, and (d)$\dot{m}$ vs P_{tr} & η

Figure 14 is the G8 compressor map of P_{tr} vs corrected mass flow rate ($\frac{\dot{m}\sqrt{T_0}}{P_0}$) with the AoAs studied superimposed to compressor speedlines ($\frac{n}{\sqrt{T_0}}$). At 20° the operating point matches the near stall condition of the speedline at 19722 $\frac{RPM}{\sqrt{T_0}}$. For AoA of 50° and greater, the operating points fall outside of the given compressor speedlines but still operate at high compressor efficiency indicating the wide range of operation the G8 compressor has. Figure 14 indicates that the G8 micro-compressor works with a range greater than the original compressor designed under uniform flow conditions. The operating line tends to be closer to the near stall boundary of the compressor. The efficiency is high, but not the highest the compressor can achieve. To maximize the compressor efficiency, the operating line should be shifted toward the right side with higher mass flow and slightly higher total pressure ratio.

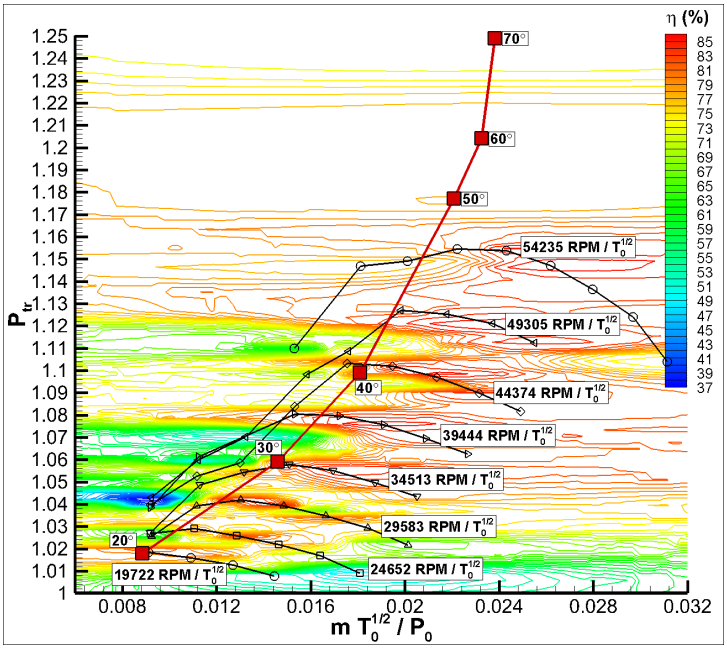

Figure 14: G8 compressor map with operating conditions

Figure 15 shows the CFJ airfoil aerodynamic performance. In Figure 15(a), the lift coefficient (C_L) increases roughly linearly with the AoA and the slope is about 3.8π rad^{-1}, substantially greater than that of thin airfoil theory of 2π rad^{-1}. Highest C_L is 13.7 at $AoA = 70°$ with a compressor RPM of 75,000. At a high AoA of 70°, the airfoil is still not stalled due to the effectiveness of the co-flow jet in overcoming the extreme adverse pressure gradients. The drag coefficient (C_D) is negative (thrust) when the AoA is greater than 30° because a large C_μ is used. Figure 15(b) shows the highest positive lift to drag ratio (C_L/C_D) of 111.7 and corrected aerodynamic efficiency $(C_L/C_D)_c$ of 13.3 for $AoA = 20°$ at micro-compressor RPM 20,000. The remaining angles have a lower $(C_L/C_D)_c$ because of the high values of P_c caused by the high compressor RPMs chosen. However, for takeoff and landing conditions the important result to note is the high C_L values obtained at high AoA.

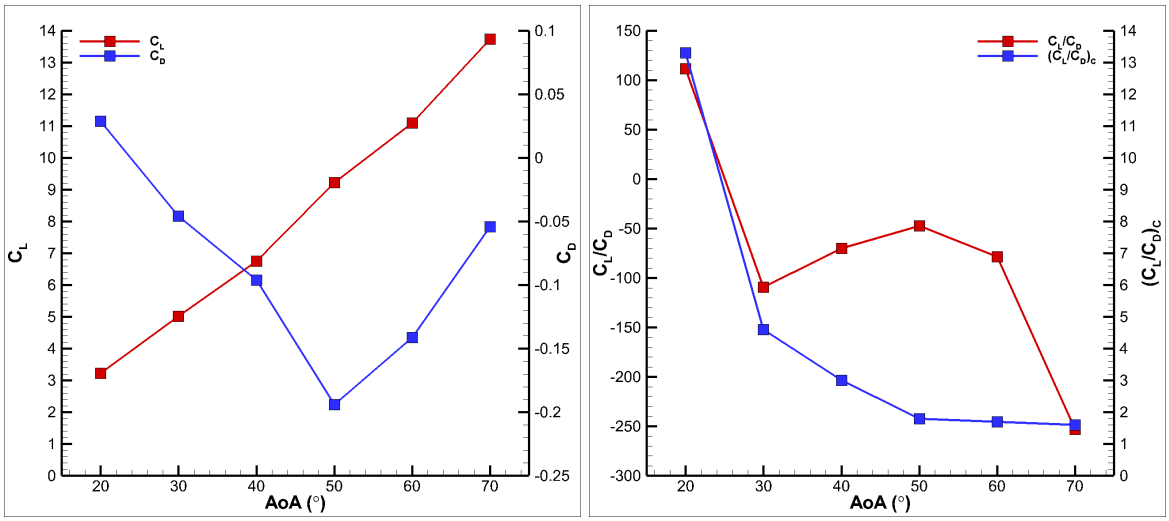

(a) (b)

Figure 15: CFJ airfoil aerodynamic performance: (a)AoA vs C_L & C_D, and (b)AoA vs C_L/C_D & $(C_L/C_D)_c$

4 Conclusion

This paper successfully conducts a 3D Co-Flow Jet (CFJ) active flow control airfoil with an integrated micro-compressor at high angles of attack for takeoff and landing conditions. The simulations indicate that the integrated CFJ airfoil has flow fully attached for AoA from 20° to 70° for takeoff and landing conditions. The RPM of the embedded micro-compressor is controlled to achieve a variety of operating conditions to satisfy the different AoA conditions.

The results show that airfoil separation can occur due to the mismatch of the micro-compressor and the airfoil flow conditions. At AoA of 20°, the compressor at higher power level with 30,000 RPM stalls both the flow of the micro-compressor and airfoil. By reducing the RPM to 20,000, the CFJ airfoil flow is nicely attached with the lift coefficient doubled and the aerodynamic efficiency $(C_L/C_D)_c$ increased by 343%. With the AoA varying from 20° to 70°, an increasing RPM of the micro-compressor actuator as well as the power is necessary to overcome the extreme adverse pressure gradient to maintain the attached flow with lift coefficient increasing from 3.2 to 13.7. The efficiency is only optimized for AoA of 20°. For all the AoAs of 30° and higher, a large C_μ is used to save simulation time without iterations to minimize the CFJ power. The aerodynamic performance of the CFJ airfoil shows a positive C_L/C_D of 111.7 and high negative values due to the generation of negative drag, which is thrust. A maximum corrected aerodynamic efficiency $(C_L/C_D)_c$ of 13.3 is obtained for the case of $AoA = 20°$ at compressor RPM 20,000 where the micro-compressor efficiency (η) is 78.2%. The highest micro-compressor efficiency obtained is 80.2% at AoA of 40° and RPM 45,000. A high lift coefficient (C_L) of 13.7 is obtained at $AoA = 70°$ at compressor RPM 75,000 where η is 72% due to significant deviation from the design RPM of 30,000. This study indicates that the CFJ airfoil can be used for high lift coefficient with high compressor efficiency. The micro-compressor actuator designed has a wide operating range with high efficiency. This study is a virtual simulation of the integrated system of the CFJ airfoil and the micro-compressor actuator to demonstrate that the CFJ airfoil can be controlled at takeoff and landing conditions for ultra-high lift coefficient and AoA.

5 Acknowledgement

The authors would like to acknowledge the computing resources provided by the Center of Computational Sciences (CCS) at the University of Miami. The teaching assistantship support from the University of Miami is also acknowledged.

Disclosure: The University of Miami and Dr. Gecheng Zha may receive royalties for future commercialization of the intellectual property used in this study. The University of Miami is also equity owner in CoFlow Jet, LLC, licensee of the intellectual property used in this study.

References

[1] G. Zha, and C.D. Paxton, "A Novel Flow Control Method for Airfoil Performance Enhancement Using Co-Flow Jet," *Applications of Circulation Control Technologies, AIAA Book Series, Progress in Aeronautics and Astronautics*, vol. Vol. 214, Chapter 10, pp. 293–314, 2006.

[2] G. Zha, W. Gao, and C.D. Paxton, "Jet Effects on Co-Flow Jet Airfoil Performance," *AIAA Journal*, vol. 45, pp. 1222–1231, 2007.

[3] G.-C. Zha, C. Paxton, A. Conley, A. Wells, and B. Carroll, "Effect of Injection Slot Size on High Performance Co-Flow Jet Airfoil," *AIAA Journal of Aircraft*, vol. 43, pp. 987–995, 2006.

[4] G.-C. Zha, B. Carroll, C. Paxton, A. Conley, and A. Wells, "High Performance Airfoil with Co-Flow Jet Flow Control," *AIAA Journal*, vol. 45, pp. 2087–2090, 2007.

[5] Wang, B.-Y. and Haddoukessouni, B. and Levy, J. and Zha, G.-C., "Numerical Investigations of Injection Slot Size Effect on the Performance of Co-Flow Jet Airfoil," *Journal of Aircraft*, vol. Vol. 45, No. 6,, pp. pp.2084–2091, 2008.

[6] B. P. E. Dano, D. Kirk, and G.-C. Zha, "Experimental Investigation of Jet Mixing Mechanism of Co- Flow Jet Airfoil." AIAA-2010-4421, 5th AIAA Flow Control Conference, Chicago, IL, 28 Jun - 1 Jul 2010.

[7] B. P. E. Dano, G.-C. Zha, and M. Castillo, "Experimental Study of Co-Flow Jet Airfoil Performance Enhancement Using Micro Discreet Jets." AIAA Paper 2011-0941, 49th AIAA Aerospace Sciences Meeting, Orlando, FL, 4-7 January 2011.

[8] A. Lefebvre, B. Dano, W. Bartow, M. Fronzo, and G. Zha, "Performance and energy expenditure of coflow jet airfoil with variation of mach number," *Journal of Aircraft*, vol. 53, no. 6, pp. 1757–1767, 2016.

[9] A. Lefebvre and G. Zha, "Numerical simulation of pitching airfoil performance enhancement using co-flow jet flow control," *AIAA 31st Applied Aerodynamics Conference*, vol. 2517, 2013.

[10] A. Lefebvre and G. Zha, "Co-flow jet airfoil trade study part i : Energy consumption and aerodynamic performance," *AIAA 32nd Applied Aerodynamics Conference*, vol. 2682, 2014.

[11] A. Lefebvre and G. Zha, "Co-flow jet airfoil trade study part ii : Moment and drag," *AIAA 32nd Applied Aerodynamics Conference*, vol. 2683, 2014.

[12] Y. Ren, P. Barrios, and G.-C. Zha, "Simulation of 3D Co-Flow Jet Airfoil with Integrated Micro-Compressor Actuator." AIAA Paper 2022-3553, AIAA Aviation 2022, AIAA Aviation 2022 Forum, Chicago, Illinois, 27-1 July 2022.

[13] P. Barrios, Y. Ren, and G.-C. Zha, "Simulation of 3D Co-Flow Jet Airfoil with Integrated Micro-Compressor Actuator at Different Cruise Flight Conditions." AIAA SciTech 2023, AIAA SciTech 2023 Forum, National Harbor, Maryland, 23-27 Jan 2023.

[14] Yang, Yunchao and Zha, Gecheng, "Super-Lift Coefficient of Active Flow Control Airfoil: What is the Limit?," *AIAA Paper 2017-1693, AIAA SCITECH2017, 55th AIAA Aerospace Science Meeting, Grapevine, Texas*, p. 1693, 9-13 January 2017.

[15] Y. Wang and G.-C. Zha, "Study of 3D Co-flow Jet Wing Induced Drag and Power Consumption at Cruise Conditions." AIAA Paper 2019-0034, AIAA SciTech 2019, San Diego, CA, January 7-11, 2019.

[16] Y. Wang, Y.-C. Yang, and G.-C. Zha, "Study of Super-Lift Coefficient of Co-Flow Jet Airfoil and Its Power Consumption." AIAA Paper 2019-3652, AIAA Aviation 2019, AIAA Applied Aerodynamics Conference, Dallas, Texas, 17-21 June 2019.

[17] Y. Wang and G.-C. Zha, "Study of Mach Number Effect for 2D Co-Flow Jet Airfoil at Cruise Conditions." AIAA Paper 2019-3169, AIAA Aviation 2019, AIAA Applied Aerodynamics Conference, Dallas, Texas, 17-21 June 2019.

[18] P. R. Spalart and S. R. Allmaras, "A one-equation turbulence model for aerodynamic flows," in *30th Aerospace Sciences Meeting and Exhibit, Aerospace Sciences Meetings, Reno, NV, USA, AIAA Paper 92-0439*, 1992.

[19] Shen, Y.Q., and Zha, G.C., "Large Eddy Simulation Using a New Set of Sixth Order Schemes for Compressible Viscous Terms," *Journal of Computational Physics*, vol. 229, pp. 8296–8312, doi:10.1016/j.jcp.2010.07.017, 2010.

[20] Zha, G.C., Shen, Y.Q. and Wang, B.Y., "An improved low diffusion E-CUSP upwind scheme ," *Journal of Computer and Fluids*, vol. 48, pp. 214–220, Sep. 2011.

[21] Y.-Q. Shen and G.-Z. Zha , "Generalized finite compact difference scheme for shock/complex flowfield interaction," *Journal of Computational Physics*, vol. doi:10.1016/j.jcp.2011.01.039, 2011.

[22] Shen, Y.Q., Zha, G.C., and Wang, B.Y., "Improvement of Stability and Accuracy of Implicit WENO Scheme," *AIAA Journal*, vol. 47, pp. 331–334, DOI:10.2514/1.37697, 2009.

[23] Shen, Y.Q., Zha, G.C., and Chen, X., "High Order Conservative Differencing for Viscous Terms and the Application to Vortex-Induced Vibration Flows," *Journal of Computational Physics*, vol. 228(2), pp. 8283–8300, doi:10.1016/j.jcp.2009.08.004, 2009.

[24] Shen, Y.Q., and Zha, G.C., "Improvement of the WENO Scheme Smoothness Estimator," *International Journal for Numerical Methods in Fluids*, vol. 64,, pp. 653–675, DOI:10.1002/fld.2186, 2009.

[25] Zha, G.C., and Bilgen, E., "Numerical Study of Three-Dimensional Transonic Flows Using Unfactored Upwind Relaxation Sweeping Algorithm," *Journal of Computational Physics*, vol. 125, pp. 425–433,, 1996.

[26] Wang, B.Y., Hu, Z. and Zha, G.C., "A General Sub-Domain Boundary Mapping Procedure For Structured Grid CFD Parallel Computation," *AIAA Journal of Aerospace Computing, Information, and Communication*, vol. 5, pp. 425–447, 2008.

[27] H. Im and G. Zha, "Investigation of flow instability mechanism causing compressor rotor-blade nonsynchronous vibration," *AIAA Journal*, vol. 52, no. 9, pp. 2019–2031, 2014.

[28] *Investigation of Mixed Micro-Compressor Casing Treatment Using Non-Matching Mesh Interface*, vol. Volume 8: Microturbines, Turbochargers, and Small Turbomachines; Steam Turbines of *Turbo Expo: Power for Land, Sea, and Air*, 06 2019. V008T26A013.

[29] Y.-Q. Shen, G.-C. Zha, and B.-Y. Wang, "Improvement of Stability and Accuracy of Implicit WENO Scheme," *AIAA Journal*, vol. 47, pp. 331–344, 2009.

[30] Y. Ren, K. Xu, and G.-C. Zha, "Design of G8 Micro-Compressor for CoFlow Jet Airfoil." Internal Report No.1, Dept. of Mechanical and Aerospace Engineering, University of Miami, May 2020.